Simulations of 2-D Materials-Based Field Effect Transistors for Quantum Cascade Detectors

Emmanuele Cannavò, Damiano Marian, Enrique Gonzalez Marin, Alessandro Tredicucci, and Gianluca Fiori

***Abstract*— We explore through numerical simulations the possibility of exploiting 2-D materials (2DMs)-based field effect transistors (FETs) as read-out devices for quantum cascade (QC) detectors. For this purpose, a deep investigation of the device parameter space has been performed while considering different 2DMs as channel material, such as graphene and transition metal dichalcogenides (TMDs), considering both short- and long-channel devices. We find that while graphene offers the highest current density for a given impinging power, it shows higher OFF-currents as compared to other solutions based on TMDs, which, eventually, can represent a better choice for this particular application.**

***Index Terms*— 2-D materials (2DMs), ballistic transport, diffusive transport, quantum cascade detector (QCD), terahertz (THz).**

I. Introduction

THE terahertz (THz) gap has, for decades, attracted intense research activity, which sought to technologically bridge the microwave and optical regions of the electromagnetic spectrum. Despite the efforts and several notable proposals [1], [2], [3], [4], [5], [6], the generalized adoption of emitters and detectors in the far- and mid-infrared wavelengths is not solved. In this field, quantum cascade (QC) technology has represented a main workhorse. QC devices leverage the quantum engineering of the electronic band structure for the detection/emission of photons with frequencies not constrained to the semiconductor bandgap energy. In particular, their operation at a specific wavelength is enabled by the proper design of the quantum wells (QWs) and the adjustment of the corresponding intersubband transitions.

Two main aims are pursued toward THz photodetection: high operation speed and high responsivity (the latter to be achieved while keeping both a low dark current and a high sensitivity). The simultaneous optimization of both figures of merit is challenging. In the timescale arena, QC detectors (QCDs) [7], [8], [9] rose to prominence as especially appealing because they operate as unipolar devices: as such, their fundamental speed limit is set by the intersubband scattering time of electrons (induced by longitudinal optical phonons), which is of the order of picoseconds.

During the rich history of QCDs [10], [11], [12], [13], [14], [15], [16], [17], [18], [19], [20], [21] responsivity improvement has remained an open question. While the design of the active region has a significant impact on the absorption and the internal quantum efficiency of the QCD, a nonnegligible contribution is due to the interface with the reading region from which the photocurrent is extracted. In particular, in QCDs, detection is usually achieved by means of direct measurements (e.g., with a two-point probe). This generally complicates the active region design (which needs to include highly doped regions working as low-resistive contacts located above and below the active region), thus impacting the collection of the photogenerated carriers, and therefore, the responsivity.

A novel alternative to conventional QCD reader designs could consist of the exploitation of electrostatic coupling of the active area with a 2-D material (2DM) channel. 2DMs are especially attractive to this end because their monoatomic thickness guarantees superior electrostatic interaction. While 2DMs have already been extensively studied both in their electronic [22], [23], [24], [25], [26], [27], [28] and in their optoelectronic properties [29], [30], [31], [32], [33], [34], [35], [36], [37], [38], these read-out architectures remain mostly unexplored [39] both from the theoretical and experimental point of view. In this case, the QCD active region would play the role of a photo-controlled gate of a Field Effect Transistor (FET) structure where the 2DM-channel coupling-induced charge would provide the electrical read-out (while the 2DM does not interact directly with the electromagnetic radiation). This design could potentially meet the need for simpler, smaller, and easily scalable detecting devices, which could find application in the THz field in tandem with THz

Manuscript received 15 September 2023; revised 24 October 2023; accepted 7 November 2023. Date of publication 20 November 2023; date of current version 2 January 2024. This work was supported in part by the European Project ERC PEP2D under Contract 770047; in part by the European Union's Horizon 2020 Research and Innovation Program under the grant agreements Graphene Flagship Core 3 under Contract 881603; and in part by the National Center for HPC, Big Data and Quantum Computing (HPC) under Project CN00000013. The review of this article was arranged by Editor Y. Chauhan. *(Corresponding author: Emmanuele Cannavò.)*

Emmanuele Cannavò and Gianluca Fiori are with the Dipartimento di Ingegneria dell'Informazione, Università di Pisa, 56126 Pisa, Italy (e-mail: emmanuele.cannavo@phd.unipi.it; gianluca.fiori@unipi.it).

Damiano Marian is with the Dipartimento di Ingegneria dell'Informazione, Università di Pisa, 56126 Pisa, Italy, and also with the Dipartimento di Fisica "E. Fermi," University of Pisa, 56127 Pisa, Italy (e-mail: damiano.marian@unipi.it).

Enrique Gonzalez Marin is with the Departamento de Electrónica y Tecnología de Computadores, Facultad de Ciencias, Universidad de Granada, 18071 Granada, Spain (e-mail: egmarin@go.ugr.es).

Alessandro Tredicucci is with the Dipartimento di Fisica "E. Fermi," University of Pisa, 56127 Pisa, Italy (e-mail: alessandro.tredicucci@unipi.it).

Color versions of one or more figures in this article are available at https://doi.org/10.1109/TED.2023.3332073.

Digital Object Identifier 10.1109/TED.2023.3332073

© 2023 The Authors. This work is licensed under a Creative Commons Attribution-NonCommercial-NoDerivatives 4.0 License.
For more information, see https://creativecommons.org/licenses/by-nc-nd/4.0/

light emitters; furthermore, the use of FETs as readers is likely to lead to an intrinsic current amplification effect in the detector.

In this work, we explore the possibility of exploiting 2DM-based FETs as readers in QCDs, looking for the 2DM-based channel that works best at detecting the photovoltage changes in the active region. To this purpose, we consider the active region architecture proposed by Schwarz et al. [13] with outstanding external quantum efficiencies of 40% at 80 K and 25% at 300 K. Different 2DMs are taken into consideration as channel materials, including graphene and two different transition metal dichalcogenides (TMDs), namely Molybdenum Disulphide (MoS_2) and Tungsten Disulphide (WS_2), all monolayers. Their photo-induced current and their responsivity are investigated in detail. In particular, we investigate both long- and short-channel devices, considering the two different transport regimes, i.e., diffusive and ballistic. The former enables a direct comparison with state-of-the-art device dimensions, while the latter projects the performance of the ultimate scaled channel FETs, where the device operation should reach faster response times, higher speeds, and lower power consumption.

The article is organized as follows. In Section II, we describe the simulated device, together with the modeling of the QCD backgate action on the reader FET and the quantitative estimation of the modulating charge in the active region. In Section III, the results of the simulations are presented and discussed. Finally, in Section IV, the conclusions are drawn.

II. Methods

The proposed device concept (Fig. 1) consists of a 2DM-based FET back-gated by an active region made of alternating InGaAs/InAlAs layers (lattice matched to InP) analogous to the one realized by Ovchinnikov et al. [27], which is capacitively coupled to a bidimensional material by means of an insulating layer of HfO_2, with a thickness of $t_{ox} = 33$ nm and relative dielectric constant of $\varepsilon_{ox} = 22$, as reported in [39]. The active region realized experimentally in [13] was embedded in a waveguide with a highly doped substrate acting as a bottom contact layer to prevent light coupling from the substrate. In order to streamline the modeling process, the active region is simplified in the in silico device representation as a single layer, whose relative dielectric constant is equivalent to the one of the original heterostructure, i.e., $\varepsilon_r = 8.023$. At the bottom of the active region, there is backgate contact, which sets the bias point of the FET structure. The influence of the biasing condition on the photo-generated current and voltage has been studied, e.g., in [14] and [39], showing that the effect can be reasonably considered small and follows an approximately linear trend. In the proposed device, the light impinging on the active region induces a charge separation between the (fixed) positive nuclei and the negative electrons, which move toward the interface with the oxide (Fig. 1). This process produces a photo-voltage (Vph), that acts as a back-gate for the 2DM-FET. For computational purposes, we choose the charge generated by the impinging light as the physical input that modulates the current in the 2DM-based FET, and we investigate the performance of the latter as a function of it.

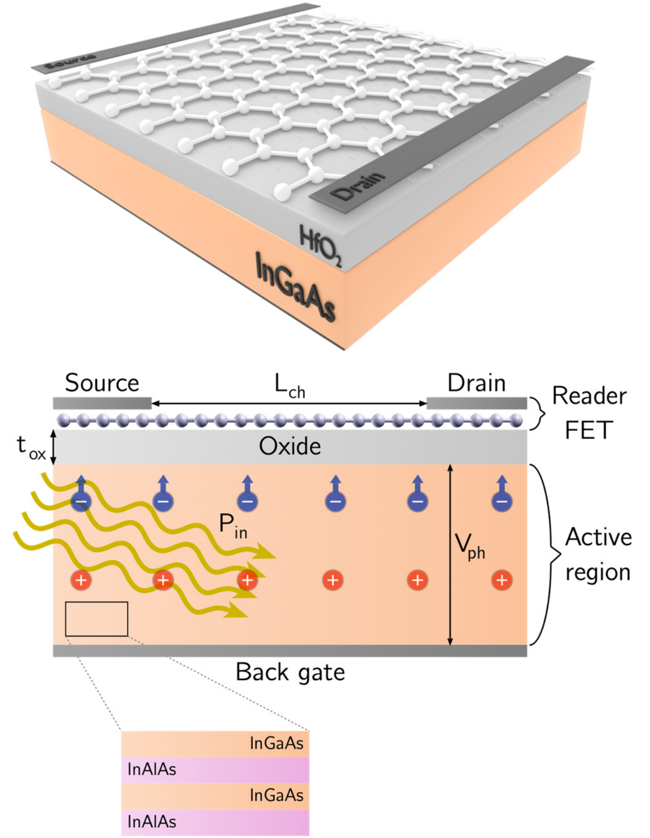

Fig. 1. Device schematics (3-D and cross section) with the relevant physical quantities highlighted; the incident power P_{in} impinges on the photodetecting active region, separating the electrons from the nuclei and generating a photovoltage V_{ph}. The induced charges act as a backgate for the reader FET.

We can relate the indirectly light-induced charge ($q\Delta n$) in the 2DM channel to the optical power (P_{in}) using the following relations:

$$q\Delta n = C_{ox}V_{ph} = C_{ox}R_0 I_{ph} = C_{ox}R_0 P_{in} R \quad (1)$$

where $C_{ox} = \varepsilon_{ox}/t_{ox}$ is the HfO_2 equivalent parallel-plate capacitance; $V_{ph} = R_0 I_{ph}$ and $I_{ph} = P_{in}R$ are the active region photogenerated voltage and current, respectively, while R_0 and R are the active region resistance and responsivity, respectively. R_0 can be determined from the active region detectivity (D_J^*). The expression for D_J^* depends on the noise: when detection takes place above the so-called "background-limited intrinsic-performance" (BLIP) temperature (124 K for this device), D_J^* is limited by the Johnson noise or thermal noise. The active region detectivity then reads as: $D_J^* = R(R_0 A_D/4k_B T)^{1/2}$, where A_D is the photodetecting area, k_B is the Boltzmann's constant, and T is the temperature. By using this expression in (1), the light-induced charge, $q\Delta n$, can be expressed in terms of D_J^*, R of the active area and the capacitive coupling due to the HfO_2 layer as

$$q\Delta n = \frac{4C_{ox}k_B T D_J^{*2}}{A_D R} P_{in}. \quad (2)$$

By using this last expression, (2), and the data from [27], we can estimate the order of magnitude of $q\Delta n$, which

TABLE I
TABLE SHOWING THE RELEVANT PARAMETERS, EFFECTIVE MASSES, EXPRESSED IN TERMS OF FREE ELECTRON MASS (m_0), AND MOBILITIES FOR THE SIMULATED DEVICES

	MoS_2	WS_2	Graphene
m_e	0.56	0.33	-
m_h	0.64	0.43	-
μ (cm^2/Vs)	25	35	2000

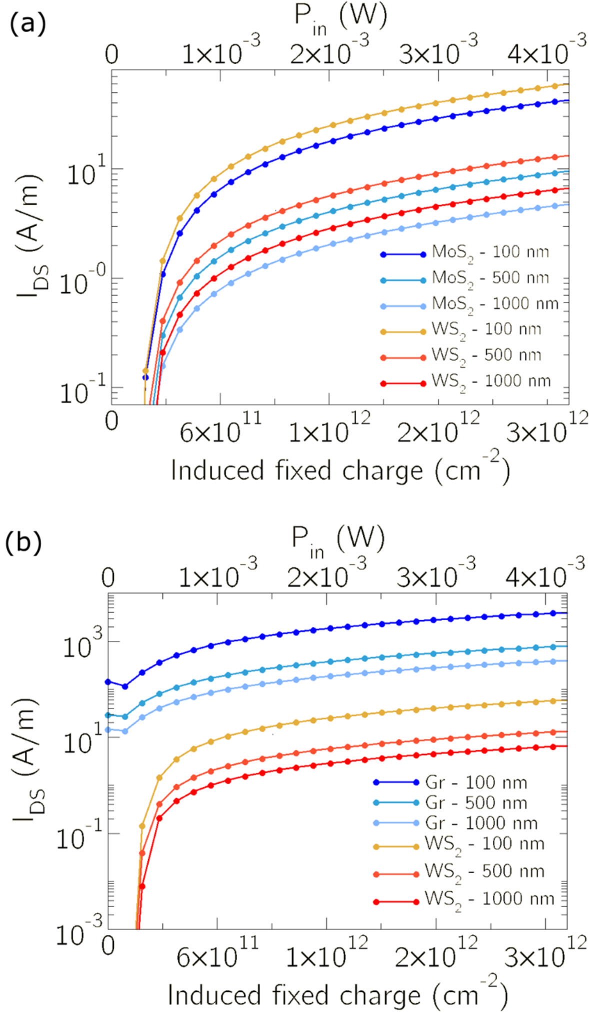

Fig. 2. (a) Comparison between the transfer characteristics in the diffusive regime for the WS_2- and MoS_2-based FET. (b) Comparison between the transfer characteristics of the graphene- and the WS_2-based FET. For all the simulated devices, we consider three different values for the channel lengths (100, 500, and 1000 nm), and V_{DS} is set to 0.2 V.

leads to readable current signals. Considering $A_D = 50\ \mu m^2$, $R = 0.86$ A/W at the chosen wavelength (4.1 μm or 73.12 THz) and $D^*_J = 7.2 \times 10^7$ (cm$\sqrt{\text{Hz}}$/W), both at room temperature [27], we obtain, for a P_{in} of the order of, say, 1 μW, a Δn of approximately 10^{12} m^{-2}. In this work, from now on, we denote the photocurrent, defined as the readable electronic response of the detector to the impinging light, as the current flowing in the 2-D channel of the read-out FET.

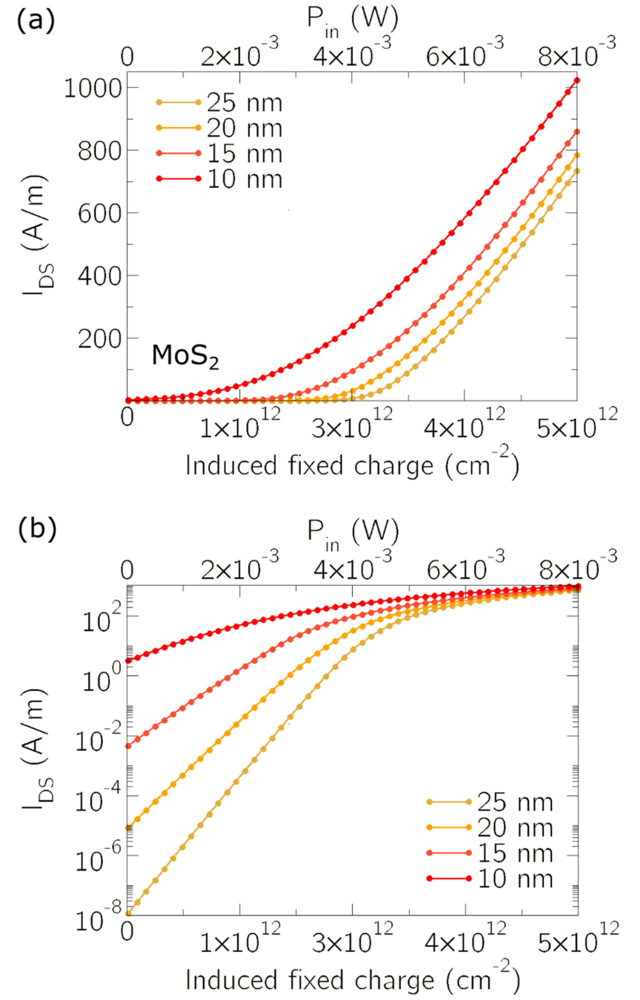

Fig. 3. Transfer characteristics for MoS_2-based FETs in the ballistic regime for different channel lengths in (a) linear and (b) semilogarithmic scale; $V_{DS} = 0.2$ V.

The electronic transport calculations in the 2DM are carried out by means of the NanoTCAD ViDES suite [41], [42], which implements both ballistic and drift-diffusion transport. In both cases, we assume invariance of the electrostatic potential along the direction perpendicular to transport; thus, in the ballistic regime, the 2-D transport equations, within the NEGF formalism, and 2-D Poisson equations, are solved self-consistently considering different values for the modulating fixed charge. The band structure of the 2DM channel is described in terms of a one orbital nearest-neighbor Hamiltonian for graphene, and an effective-mass-like Hamiltonian in the case of the different TMDs. In the drift regime, the 2-D Poisson and 2-D continuity equations, under the drift-diffusion approximation, are self-consistently solved [25], [28]. In this case, to evaluate the carrier density in the 2DM, a linear dispersion relationship close to the Dirac energy is assumed for graphene while a parabolic $E-k$ curve around the conduction band minima and valence band maxima is assumed for the TMDs. The effective masses used for the simulations (expressed in units of the free electron mass, m_0, for electrons and holes, respectively) are 0.56 and 0.64 for MoS_2 and 0.33 and 0.43 for WS_2 [22]. For graphene, a Fermi velocity of 10^6 m/s is considered.

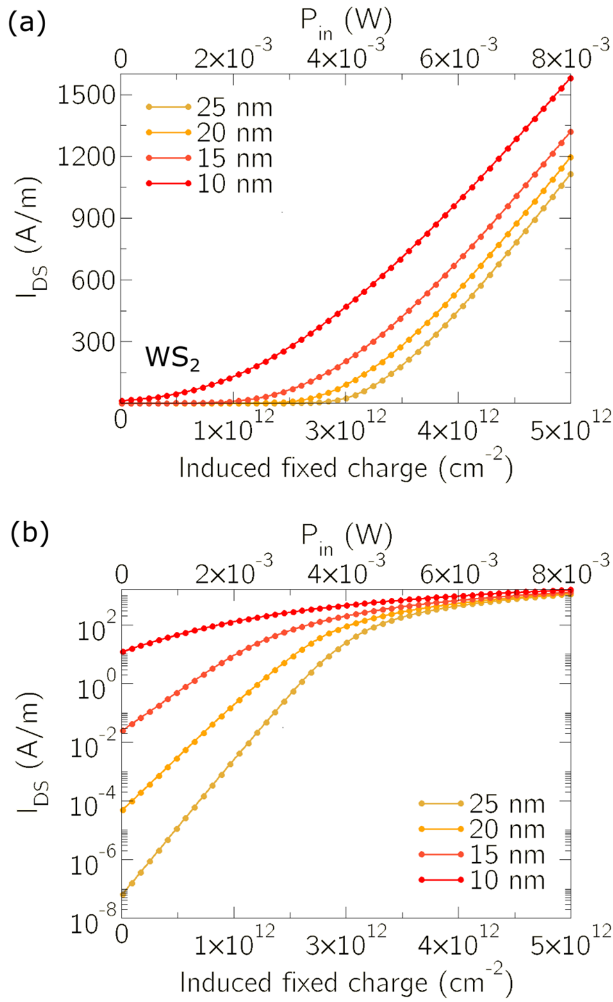

Fig. 4. Transfer characteristics for WS_2-based FETs in the ballistic regime for different channel lengths in (a) linear and (b) semilogarithmic scale; $V_{DS} = 0.2$ V.

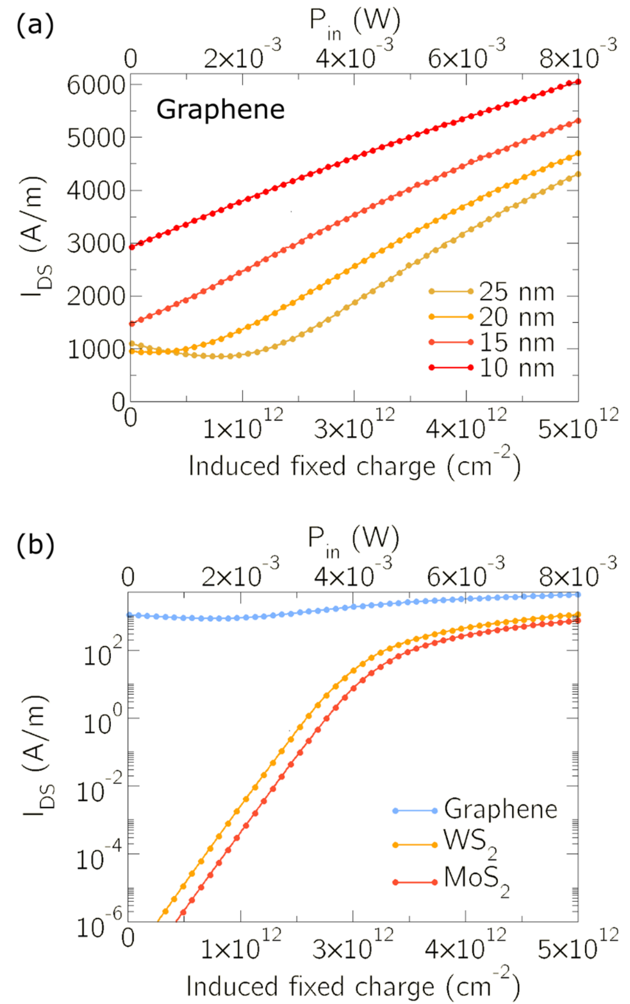

Fig. 5. Transfer characteristics in the ballistic regime for (a) graphene-based FET for different channel lengths and (b) graphene and TMDs at 25 nm channel length; $V_{DS} = 0.2$ V.

Regarding the drift simulation, mobility values of 25, 35, and 2000 $cm^2/(Vs)$ were used for MoS_2, WS_2, and graphene, respectively [26], [27] (see Table I).

The purpose of this work is to simulate the detector response under ideal device conditions; this means that the effects of unintentional doping and/or impurities in the channel region on the current response have not been taken into account. In both regimes, we, furthermore, consider a steady state photon rate, only positive photo-induced charge in the active region of the device, and we do not consider thermal noise in the detector, except that in the expression for the detectivity.

III. Results

In order to put the proposed design in the context of state-of-the-art QCDs, we have first considered device dimensions in the mesoscopic scale. In Fig. 2(a), we report the drain-to-source current obtained considering diffusive transport as a function of the modulating photo-generated charge (bottom axis) and the impinging power (top axis) for MoS_2 and WS_2 in the semi-logarithmic scale for different channel lengths, ranging from 100 nm up to a 1000 nm. The drain-to-source voltage (V_{DS}) is set to 0.2 V for all the simulations. Similar results have been obtained for two other TMDs, $MoSe_2$ and WSe_2, in the same transport regime (not reported in the picture), due to the small differences in terms of mobility, bandgap and effective mass values. First, we observe for both TMDs an increasing current for increasing values of P_{in} and the modulating fixed charge. In addition, we note, as expected, a proportional decrease in the current with increasing channel length, while the corresponding charge for which the channel can be considered in the inversion region is approximately the same for all channel lengths. As expected, WS_2 slightly outperforms MoS_2 in terms of ON-current for the same impinging power due to the large mobility considered in the simulations.

In Fig. 2(b), we compare the drift current responses of WS_2 with the analogous graphene ones, considering the same device architecture and the same channel lengths. It can be observed that, due to the higher mobility, graphene-based devices show larger currents as compared to the WS_2 ones for any considered length. On the other side, the dark current (defined as the current response at zero impinging power/induced charge) is much lower for the TMDs than for graphene (a difference of several orders of magnitude is observed), since a device

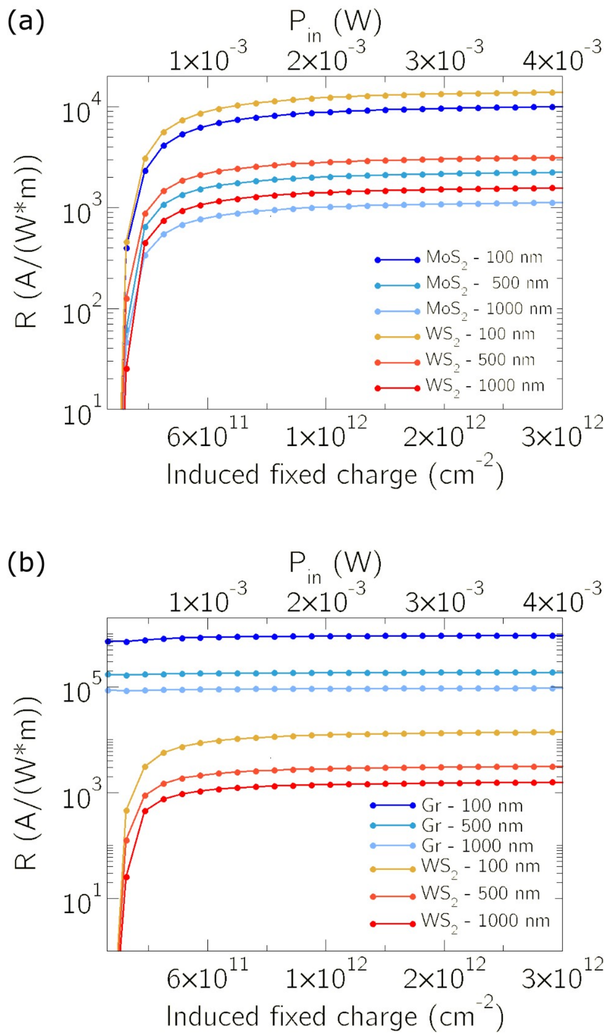

Fig. 6. (a) Comparison between the responsivities in the diffusive regime for the WS_2- and MoS_2-based FET. (b) Same as above for graphene- and the WS_2-based FET. For all the simulated devices, we consider three different values for the channel lengths (100, 500, and 1000 nm), and V_{DS} is set to 0.2 V.

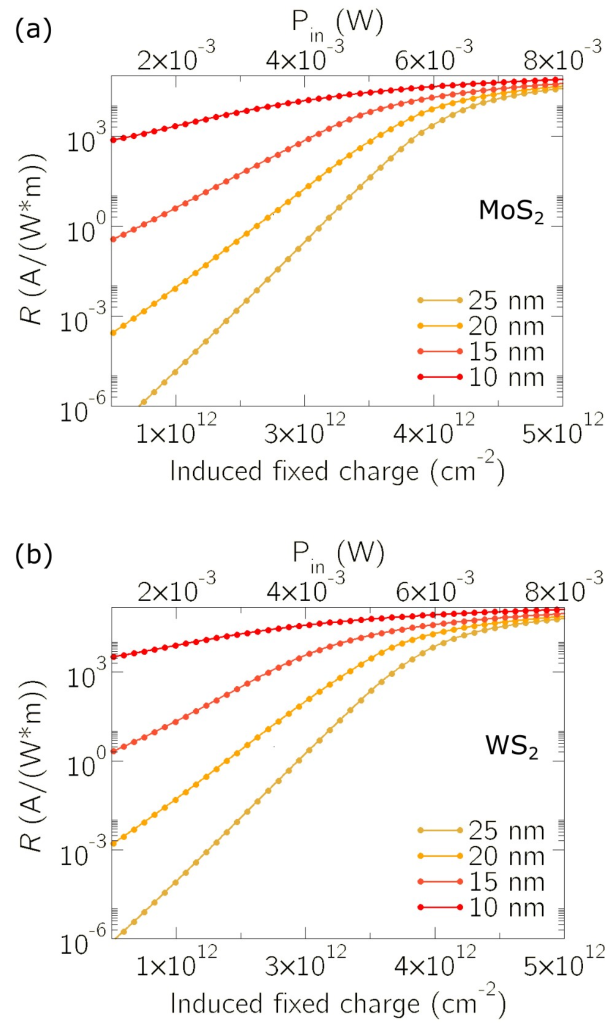

Fig. 7. Responsivity in semilogarithmic scale for different channel lengths for (a) MoS_2 and (b) WS_2; V_{DS} = 0.2 V, ballistic transport conditions.

with a graphene channel never switches off, differently to what happens in TMDs.

Next, in order to investigate the ultimate potential performance of these devices, we have considered shorter channel lengths. To this aim, we have performed transport simulations in the ballistic regime as detailed in the methods section. In Fig. 3(a) and (b), the drain-to-source currents for MoS_2, considering four different channel lengths ranging from 10 nm up to 25 nm, are shown.

As expected, in the TMDs, we see an increasing monotonic current trend with P_{in} with the modulating charge. Analogously to the drift transport case, the dark current decreases with increasing channel length since in the quantum ballistic case, longer channels lead to reduced interband tunneling in the OFF-state.

In Fig. 4(a) and (b), we show the transfer characteristics for WS_2: W-based devices feature slightly higher currents than the Mo-based also in the ballistic case. The dark current behavior for WS_2 is analogous to the MoS_2 case, with the values being of the same order of magnitude.

In Fig. 5(a), we show the analogous pictures for graphene devices. GFETs, while still showing a decreasing trend for the dark current as a function of channel length, feature a much higher current (of the order of 10^3 A/m) at zero impinging power.

The shift of I–V characteristics on the left with reduced channel length is due to the increased electrostatic control of the drain over the channel region, i.e., a short channel effect analogous to the drain-induced barrier lowering (DIBL) observed in ultrashort devices, as also reported in [43].

In Fig. 5(b), we compare the transfer characteristics for the two considered TMDs (MoS_2 and WS_2) with the one of graphene for a 25 nm channel length and V_{DS} = 0.2 V. The graphene current is noticeably higher than the TMDs for all the impinging powers considered. In particular, the current intensity for zero photovoltage flowing through graphene is more than four times higher than both the Tungsten- and the Molybdenum-based devices. As can be seen from the pictures, the current-power correlation is strongly nonlinear; calibration of real-life devices featuring this behavior is nontrivial but feasible, as demonstrated in [44].

In order to further investigate the performance of the studied devices, we have calculated the responsivity per unit width,

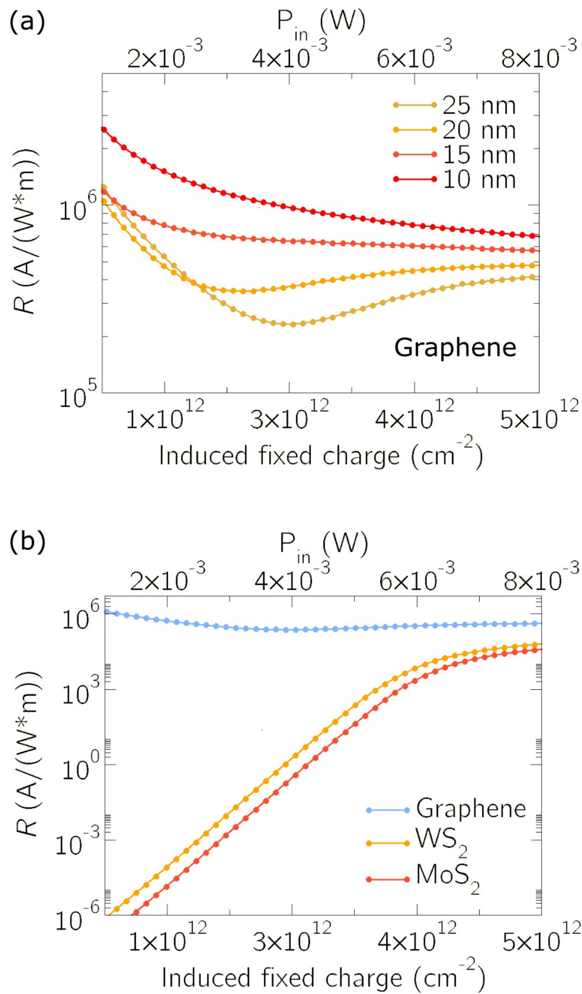

Fig. 8. (a) Responsivity in semilogarithmic scale for different channel lengths of Graphene. (b) Comparison of the responsivity for Graphene, MoS_2, and WS_2 materials at 25 nm channel length; $V_{DS} = 0.2$ V, ballistic transport conditions.

defined as $R = I_{ph}/P_{in}$, for MoS_2, WS_2, and graphene as a function of the induced fixed charge/impinging power. In Fig. 6, we report the responsivity values for the three materials and three channel lengths considered in the drift-diffusion conditions, while in Figs. 7 and 8, we do the same for the ballistic case. As can be seen, in the drift-diffusion case, the responsivity for graphene is approximately constant, while for the TMDs, it increases sharply at lower P_{in} and then starts saturating at around 1 mW of impinging power; in the ballistic case, graphene shows a general decreasing behavior for increasing P_{in} (except for the longer channel lengths, where instead a minimum is observed). In both transport regimes, graphene responsivity ranges from 10^5 to 10^6 A/(Wm). For the TMDs-based devices, we notice the highest values are instead of the order of 10^3–10^4 A/(Wm), and this is maintained in both regimes. Considering a TMD-based device whose width is of the order of 1 μm width and a length of 10 nm, its responsivity is of the order of the mA/W, which is in line with the recent literature [19], [20]. It is interesting to notice how responsivity values are preserved even at the nanoscale.

IV. Conclusion

We have modeled a 2-D-based FET where the channel material, instead of directly detecting the radiation, acts as a read-out for a QCD, performing transport simulations while spanning among the device space parameters, i.e., considering two different TMDs (MoS_2 and WS_2), different values for the channel length and comparing their performance with respect to graphene-based photodetectors. WS_2 seems to be more suited than graphene for this specific application. Indeed, although it shows lower ON-current and lower responsivity than graphene-based devices it allows, due to the low dark current, to clearly distinguish the optical input. On the other side, in the case of graphene, even if superior responsivity and ON-current are achieved compared to the TMDs-based devices, the poor modulation of the current from the induced charge and the high dark current does not allow to distinguish the impinging power. Finally, we have observed that the responsivity of the TMDs is of the order of the mA/W, even for short devices, opening the path for having simpler, smaller, and easily scalable detecting devices.

References

[1] R. E. Miles, P. Harrison, and D. Lippens, *Terahertz Sources and Systems* (NATO Science Series II). Dordrecht, The Netherlands: Kluwer, 2001.
[2] S. G. Pavlov et al., "Stimulated emission from donor transitions in silicon," *Phys. Rev. Lett.*, vol. 84, no. 22, pp. 5220–5223, May 2000, doi: 10.1103/physrevlett.84.5220.
[3] R. Köhler et al., "Terahertz semiconductor-heterostructure laser," *Nature*, vol. 417, no. 6885, pp. 156–159, May 2002, doi: 10.1038/417156a.
[4] M. Karaliūnas et al., "Non-destructive inspection of food and technical oils by terahertz spectroscopy," *Sci. Reports*, vol. 8, p. 18025, Dec. 2018, doi: 10.1002/lpor.201000011.
[5] H.-B. Liu, H. Zhong, N. Karpowicz, Y. Chen, and X.-C. Zhang, "Terahertz spectroscopy and imaging for defense and security applications," *Proc. IEEE*, vol. 95, no. 8, pp. 1514–1527, Aug. 2007, doi: 10.1109/JPROC.2007.898903.
[6] L. Masini et al., "Terahertz quantum cascade dipole-antenna vertically emitting continuous wave laser," in *Proc. Conf. Lasers Electro-Optics (CLEO)*, San José, CA, USA, 2017, pp. 1–2.
[7] F. R. Giorgetta et al., "Quantum cascade detectors," *IEEE J. Quantum Electron.*, vol. 45, no. 8, pp. 1039–1052, Aug. 2009, doi: 10.1109/JQE.2009.2017929.
[8] D. Hofstetter, M. Beck, and J. Faist, "Quantum-cascade-laser structures as photodetectors," *Appl. Phys. Lett.*, vol. 81, no. 15, pp. 2683–2685, Oct. 2002, doi: 10.1063/1.1512954.
[9] L. Gendron, C. Koeniguer, V. Berger, and X. Marcadet, "High resistance narrow band quantum cascade photodetectors," *Appl. Phys. Lett.*, vol. 86, no. 12, p. 12116, Mar. 2005, doi: 10.1063/1.1884257.
[10] A. Jollivet et al., "Short infrared wavelength quantum cascade detectors based on m-plane ZnO/ZnMgO quantum wells," *Appl. Phys. Lett.*, vol. 113, Dec. 2018, Art. no. 251104, doi: 10.1063/1.5058120.
[11] A. Bigioli et al., "Long-wavelength infrared photovoltaic heterodyne receivers using patch-antenna quantum cascade detectors," *Appl. Phys. Lett.*, vol. 116, Apr. 2020, Art. no. 161101, doi: 10.1063/5.0004591.
[12] A. Harrer et al., "43 μm quantum cascade detector in pixel configuration," *Opt. Exp.*, vol. 24, no. 15, p. 17041, Jul. 2016, doi: 10.1364/oe.24.017041.
[13] B. Schwarz et al., "The limit of quantum cascade detectors: A single period device," *Appl. Phys. Lett.*, vol. 111, no. 6, p. 061107, Aug. 2017, doi: 10.1063/1.4985711.
[14] A. P. Ravikumar, T. A. Garcia, J. D. Jesus, M. C. Tamargo, and C. F. Gmachl, "High detectivity short-wavelength II-VI quantum cascade detector," *Appl. Phys. Lett.*, vol. 105, no. 6, Aug. 2014, Art. no. 061113, doi: 10.1063/1.4893359.
[15] A. P. Ravikumar, J. De Jesus, M. C. Tamargo, and C. F. Gmachl, "High performance, room temperature, broadband II-VI quantum cascade detector," *Appl. Phys. Lett.*, vol. 107, no. 14, Oct. 2015, Art. no. 141105, doi: 10.1063/1.4932538.

[16] Y. Song, R. Bhat, T.-Y. Huang, P. Badami, C.-E. Zah, and C. Gmachl, "III-nitride quantum cascade detector grown by metal organic chemical vapor deposition," *Appl. Phys. Lett.*, vol. 105, no. 18, Nov. 2014, Art. no. 182104, doi: 10.1063/1.4901220.

[17] P. Reininger et al., "Quantum cascade detector utilizing the diagonal-transition scheme for high quality cavities," *Opt. Exp.*, vol. 23, no. 5, p. 6283, Mar. 2015, doi: 10.1364/oe.23.006283.

[18] J.-H. Son, S. J. Oh, and H. Cheon, "Potential clinical applications of terahertz radiation," *J. Appl. Phys.*, vol. 125, no. 19, May 2019, Art. no. 190901, doi: 10.1063/1.5080205.

[19] K. Li et al., "High responsivity quantum cascade detectors with bound-to-miniband diagonal transition," *Appl. Phys. Lett.*, vol. 119, no. 5, Aug. 2021, Art. no. 051101, doi: 10.1063/5.0058094.

[20] K. Li et al., "Quantum cascade detectors with enhanced responsivity using coupled double-well structures," *Appl. Phys. Exp.*, vol. 15, no. 3, Mar. 2022, Art. no. 032005, doi: 10.35848/1882-0786/ac5500.

[21] A. Harrer et al., "Mid-infrared surface transmitting and detecting quantum cascade device for gas-sensing," *Sci. Rep.*, vol. 6, p. 21795, Feb. 2016, doi: 10.1038/srep21795.

[22] J. Chang, L. F. Register, and S. K. Banerjee, "Ballistic performance comparison of monolayer transition metal dichalcogenide MX_2 (M = Mo, W; X = S, Se, Te) metal-oxide-semiconductor field effect transistors," *J. Appl. Phys.*, vol. 115, Feb. 2014, Art. no. 084506, doi: 10.1063/1.4866872.

[23] W. Zhou et al., "Designing sub-10-nm metal-oxide-semiconductor field-effect transistors via ballistic transport and disparate effective mass: The case of two-dimensional BiN," *Phys. Rev. Appl.*, vol. 13, no. 4, Apr. 2020, Art. no. 044066, doi: 10.1103/physrevapplied.13.044066.

[24] M. Chhowalla, D. Jena, and H. Zhang, "Two-dimensional semiconductors for transistors," *Nature Rev. Mater.*, vol. 1, no. 11, pp. 1–15, Aug. 2016, doi: 10.1038/natrevmats.2016.52.

[25] M. Perucchini, D. Marian, E. G. Marin, T. Cusati, G. Iannaccone, and G. Fiori, "Electronic transport in 2D-based printed FETs from a multiscale perspective," *Adv. Electron. Mater.*, vol. 8, no. 5, Jan. 2022, Art. no. 2100972, doi: 10.1002/aelm.202270023.

[26] N. Huo, Y. Yang, Y.-N. Wu, X.-G. Zhang, S. T. Pantelides, and G. Konstantatos, "High carrier mobility in monolayer CVD-grown MoS_2 through phonon suppression," *Nanoscale*, vol. 10, no. 31, pp. 15071–15077, Jul. 2018, doi: 10.1039/c8nr04416c.

[27] D. Ovchinnikov, A. Allain, Y.-S. Huang, D. Dumcenco, and A. Kis, "Electrical transport properties of single-layer WS_2," *ACS Nano*, vol. 8, no. 8, pp. 8174–8181, Jul. 2014, doi: 10.1021/nn502362b.

[28] P. K. Dubey, D. Marian, and G. Fiori, "Multiscale simulations of 2-D material ink-based printed network devices," *IEEE Trans. Electron Devices*, vol. 70, no. 2, pp. 689–694, Feb. 2023, doi: 10.1109/TED.2022.3232082.

[29] W. Chen et al., "Scaling analysis of high gain monolayer MoS_2 photodetector for its performance optimization," *IEEE Trans. Electron Devices*, vol. 63, no. 4, pp. 1608–1614, Apr. 2016, doi: 10.1109/TED.2016.2532908.

[30] G. Konstantatos, "Current status and technological prospect of photodetectors based on two-dimensional materials," *Nature Commun.*, vol. 9, no. 1, p. 5266, Dec. 2018, doi: 10.1038/s41467-018-07643-7.

[31] K. Yoshioka, T. Wakamura, M. Hashisaka, K. Watanabe, T. Taniguchi, and N. Kumada, "Ultrafast intrinsic optical-to-electrical conversion dynamics in a graphene photodetector," *Nature Photon.*, vol. 16, p. 718, Aug. 2022, doi: 10.1038/s41566-022-01058-z.

[32] H. Jiang et al., "Enhanced photogating effect in graphene photodetectors via potential fluctuation engineering," *ACS Nano*, vol. 16, p. 4458, Feb. 2022, doi: 10.1021/acsnano.1c10795.

[33] F. Bianco et al., "Terahertz detection by epitaxial-graphene field-effect-transistors on silicon carbide," *Appl. Phys. Lett.*, vol. 107, no. 13, Sep. 2015, Art. no. 131104, doi: 10.1063/1.4932091.

[34] A. Di Gaspare et al., "Graphene-based field effect transistors for radiation-induced field sensing," *Nucl. Instrum. Methods Phys. Res. A, Accel. Spectrom. Detect. Assoc. Equip.*, vol. 824, pp. 392–393, Jul. 2016, doi: 10.1016/j.nima.2015.08.066.

[35] C. Liu et al., "Room-temperature high-gain long-wavelength photodetector via optical-electrical controlling of hot carriers in graphene," *Adv. Opt. Mater.*, vol. 6, Oct. 2018, Art. no. 1800836, doi: 10.1002/adom.201800836.

[36] G. Batignani et al., "Development of graphene-based ionizing radiation sensors," *Nucl. Instrum. Methods Phys. Res. A, Accel. Spectrom. Detect. Assoc. Equip.*, vol. 936, pp. 666–668, Aug. 2019, doi: 10.1016/j.nima.2018.08.088.

[37] G. Auton et al., "Terahertz detection and imaging using graphene ballistic rectifiers," *Nano Lett.*, vol. 17, no. 11, pp. 7015–7020, Oct. 2017, doi: 10.1021/acs.nanolett.7b03625.

[38] A. Zak et al., "Antenna-integrated 0.6 THz FET direct detectors based on CVD graphene," *Nano Lett.*, vol. 14, no. 10, pp. 5834–5838, Sep. 2014, doi: 10.1021/nl5027309.

[39] G. Germanese, "Mid-infrared quantum cascade detector with graphene field-effect read-out," Master thesis, Dipartimento di Fisica, Università di Pisa, Pisa, Italy, 2019.

[40] H. Schenider and H. C. Liu, *Quantum Well Infrared Photodetectors: Physics and Applications*. Berlin, Germany: Springer, 2007.

[41] *NanoTCAD ViDES*. Accessed: Nov. 17, 2023. [Online]. Available: http://vides.nanotcad.com

[42] D. Marian, E. G. Marin, M. Perucchini, G. Iannaccone, and G. Fiori, "Multi-scale simulations of two dimensional material based devices: The NanoTCAD ViDES suite," *J. Comput. Electron.*, vol. 22, no. 5, pp. 1327–1337, Jun. 2023, doi: 10.1007/s10825-023-02048-2.

[43] S.-J. Han, Y. Sun, A. A. Bol, W. Haensch, and Z. Chen, "Study of channel length scaling in large-scale graphene FETs," in *Proc. Symp. VLSI Technol.*, Honolulu, HI, USA, Jun. 2010, pp. 231–232, doi: 10.1109/VLSIT.2010.5556239.

[44] S. C. Cain, "Non-linear statistical photocalibration of photodetectors without calibrated light sources," *Appl. Opt.*, vol. 59, no. 9, p. 2767, Mar. 2020, doi: 10.1364/ao.385753.

Open Access funding provided by 'Università di Pisa' within the CRUI CARE Agreement